Enhancing hyperspectral imaging through macro and multi-modal capabilities

Journal of Physics: Photonics

PAPER

Enhancing hyperspectral imaging through macro and multi-modal capabilities

Benedetto Ardini[1], **Matteo Corti**[1], **Marta Ghirardello**[1], **Alessia Di Benedetto**[1], **Letizia Berti**[2,3], **Cristina Cattò**[4], **Sara Goidanich**[3], **Giorgia Sciutto**[5], **Silvia Prati**[5], **Gianluca Valentini**[1,6], **Cristian Manzoni**[6], **Daniela Comelli**[1,*] and **Alessia Candeo**[1]

[1] Department of Physics, Politecnico di Milano, Piazza Leonardo da Vinci, 32, 20133 Milano, Italy
[2] Department of Sciences of Antiquity, University of Rome La Sapienza, Piazzale Aldo Moro, 5, 00185 Rome, Italy
[3] Department of Chemistry, Materials and Chemical Engineering 'Giulio Natta', Politecnico di Milano, Piazza Leonardo Da Vinci 32, Milan, 20133, Italy
[4] Department of Food, Environmental and Nutritional Sciences, Università degli Studi di Milano, Via Celoria 2, 20133 Milan, Italy
[5] Department of Chemistry, Università di Bologna, Ravenna Campus, Via Guaccimanni 42, 48121 Ravenna, Italy
[6] IFN-CNR, Piazza Leonardo da Vinci 32, 20133 Milan, Italy
[*] Author to whom any correspondence should be addressed.

E-mail: daniela.comelli@polimi.it

Keywords: hyperspectral imaging, Fourier transform, macro imaging, heritage science

Supplementary material for this article is available online

OPEN ACCESS

RECEIVED
22 December 2023

REVISED
19 April 2024

ACCEPTED FOR PUBLICATION
16 May 2024

PUBLISHED
3 June 2024

Abstract

Hyperspectral imaging (HSI) has emerged as an effective tool to obtain spatially resolved spectral information of artworks by combining optical imaging with spectroscopy. This technique has proven its efficacy in providing valuable information both at the large and microscopic scale. Interestingly, the macro scale has yet to be thoroughly investigated using this technology. While standard HSI methods include the use of spatial or spectral filters, alternative methods based on Fourier-transform interferometry have also been utilised. Among these, a hyperspectral camera employing a birefringent common-path interferometer, named TWINS, has been developed, showing a high robustness and versatility. In this paper, we propose the combination of TWINS with a macro imaging system for the study of cultural heritage (CH). We will show how the macro-HSI system was designed, and we will demonstrate its efficient capabilities to collect interferometric images with high visibility and good signal of both reflectance and fluorescence on the same field of view, even on non-flat samples. Our hyperspectral camera for macro studies of both reflectance and fluorescence data is a completely new asset in the CH panorama and beyond. The relevance of the macro technology is demonstrated in two case studies, aiding in the analysis of biofilms on stone samples and of the degradation of dyed textiles.

1. Introduction

In the last 50 years, scientific and technological advancements have played a pivotal role in changing the way cultural heritage (CH) artworks are studied [1–3]. Scientific methodologies, ranging from cutting-edge imaging technologies to meticulous material analysis, have become indispensable tools in the hands of conservators and archaeologists, helping them in getting valuable information on the preservation status of the CH objects [4–6] and in unravelling the mysteries of historical artifacts and artworks [7–9]. Among the different non-invasive techniques, hyperspectral imaging (HSI) has emerged as an effective tool, providing remarkable insights into the study of diverse artifacts and historical objects [10, 11]. This advanced imaging technique goes beyond the limitations of traditional photography by capturing a broad spectrum of wavelengths, allowing for the collection of detailed information related with the materials present on the surface of the studied object [12, 13].

In conservation science, HSI is typically applied at either the large scale, for the entire object, where the size of the FOV is tens or hundreds of centimetres, or at the microscopic scale, to investigate the local

distributions of materials, as pigment grains in the paint layer, in a FOV of hundreds of micrometres. The first approach allows for the study of full-scale works of art [14, 15] but sacrifices the ability to examine small details. In contrast, the second approach provides high-resolution insights into microscopic samples taken from artworks [16, 17]. However, it proves inadequate for studying non-flat samples due to the short depth of focus of microscopy objectives. Moreover, it requires the extraction of a sample from the object of interest, losing the contextual information.

On the contrary, there are limited examples of the use of HSI with FOV of intermediate size, i.e. with sizes close to the one achieved in close-up or macro photography. To our knowledge we can report only a reflectivity study by Picollo and coauthors on photographic films [10]. Therein, an HSI scanner was modified to achieve a spatial resolution of hundreds of micrometres and allow the study of sub-millimetric details on 35 mm photographic negatives and positives. Thanks to the excellent spatial and spectral resolution of the developed HSI system, the research paved the way for extending this approach to the study of further types of CH objects.

When reviewing the literature on the application of HSI in CH contexts, a further limitation becomes apparent: HSI systems are primarily utilized for collecting reflectivity data. However, an interesting opportunity lies in the potential use of HSI to gather multimodal datasets related to different optical phenomena. While there are some instances where reflectivity and optical fluorescence spectral datasets of the same artwork have been sequentially collected with the same HSI camera [18–20], such examples are limited. Adopting a multimodal approach holds promise in significantly enhancing our ability to characterize the materials present in works of art.

Standard methods for collecting HSI data are based on three main approaches [21]: line-scanning imaging spectrometers, filter-based imaging systems and snapshot hyperspectral cameras. Line-scanning imaging spectrometers produce spectral datacubes by moving objects or detectors over one spatial coordinate, while the spectral sensitivity is given by a compact spectrometer in the detection scheme. Filter-based imaging systems construct datacubes as stacks of images by filtering incoming light in discrete spectral bands. With snapshot cameras the datacube is readout entirely in one shot without the need of spectral or spatial scanning, typically at a price of a limited spatial and spectral resolution. It must be noted that all these methods are based on filtering of the incoming light through either bandpass or dispersive elements. A different approach is Fourier transform HSI (FT-HSI) that uses interferometry and FT operation to retrieve spectral information [22]. FT-HSI offers advantages over traditional HSI techniques, including higher signal-to-noise ratio, greater flexibility in FOV, and flexible spectral resolution. Recently, an ultra-stable common-path interferometer named TWINS was introduced and employed in combination with a monochrome camera to perform HSI analysis [23]. The TWINS-HSI camera has a spectral resolution adjustable down to 4 nm and, thanks to its common-path arrangement, is interferometrically robust against mechanical vibrations. Thanks to its small power consumption and compact footprint the TWINS interferometer can be embedded in a variety of imaging systems and employed in different configurations [24–27], including microscopy and *in situ* analysis platforms.

In this paper, we present the combination of the TWINS-HSI camera with a carefully designed optical system that enables the examination of a centimetre-sized FOV. Hereafter this implementation will be referred to as the 'macro-HSI' configuration. The designed optical system allows one to switch from the standard HSI to the macro-HSI configuration for the inspection of FOV with lateral dimensions of tens of millimetres. This innovative approach not only broadens the scope of HSI applications but also extends its versatility. Throughout this paper, we will elucidate the design concept behind it, and we will compare the macro configuration to the standard one. Furthermore, we will demonstrate how, thanks to the high light throughput of the TWINS-HSI camera, the designed system enables the sequential acquisition of HSI datasets of both reflectance and fluorescence from samples, even for objects with uneven surfaces, allowing the effective implementation of a multimodal approach. We will indeed showcase its successful application to two case studies, demonstrating how this technology can aid the study of biofilms (sessile microorganisms) on stone samples and the monitoring of the degradation of dyed textiles.

2. Materials and methods

2.1. Macro-HSI with TWINS configuration

The implementation of the TWINS as a hyperspectral camera has been detailed in depth in other publications [23, 27]. Here we explore the capability of the TWINS-HSI to be used in a macro configuration, while maintaining its high light throughput and contrast. In the standard configuration of the TWINS-HSI camera, the TWINS interferometer is placed in front of the 25 mm camera lens of a monochrome 2D silicon detector with sensitivity spanning from 400 nm to 1000 nm (figure 1(A)). In this design, the imaging system

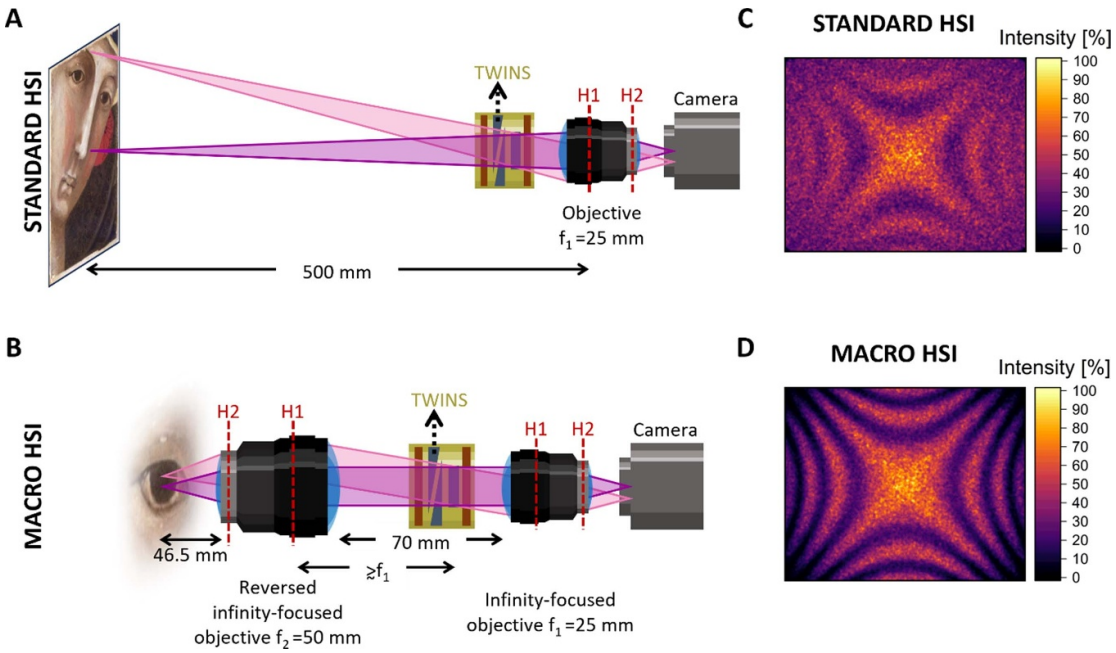

Figure 1. Scheme of the standard and macro-HSI systems. (A) Standard configuration of the TWINS-HSI camera, in which the TWINS interferometer is placed in front of a monochrome camera coupled with a 25 mm camera lens, and the sample is positioned at least 500 mm from it. The TWINS is made of two crossed polarisers, two birefringent wedges with orthogonal optical axis and birefringent plate. To vary the delay between the two light replicas, one of the two wedges is shifted. (B) Macro-HSI configuration of the hyperspectral camera used in the presented experiments, where an additional photographic objective is placed in a reverse manner in front of the standard TWINS-HSI camera at a distance larger than the ideal one, i.e. larger than the sum of the single focal lengths of the two objectives. (C) Simulated zero-path-delay for the standard configuration. (D) Simulated zero-path-delay for the macro-HSI configuration.

can be placed at a minimum working distance from the object surface of 50 cm and has an angular FOV of 16°. At such distance, this corresponds to a FOV size of 15 cm.

An important figure of merit of the TWINS-HSI camera is the high fringe contrast of each interferogram, whose FT provides the intensity spectrum. A high contrast is obtained when the bundle of rays converging to each image point is collimated while crossing the interferometer. In a macro-HSI configuration this property requires a two-lens optical system, as shown in figure 1(B). More specifically, the TWINS must be placed in the back focal plane of the first objective lens, so that its clear aperture is the aperture stop of an optical system which is telecentric in the object space. The second objective lens focuses the parallel ray bundles to the detector. Since the latter is placed in the back focal plane of the second objective, it is conjugated to the front focal plane of the first objective, i.e. the object plane. If also the second objective lens is at a distance from the TWINS equal to its focal length, the optical system is commonly called 4 f. Beyond granting high fringe contrast, this optical scheme has additional advantages. In fact, the effective angular aperture of the system is the same in all points of the FOV, so that no vignetting is present in the image. Additionally, using an iris in front of the TWINS, its clear aperture can be reduced to increase the depth of field of the system, a property which is required when imaging 3D objects. As in all telecentric systems, this is at the expense of light-harvesting power, which must be compensated for by higher irradiance or excitation power density in the plane of the object when measuring reflectance or fluorescence, respectively.

In our implementation of the macro-HSI, the first lens is a photographic Nikon objective (Nikon Nikkor, 50 mm $f/1.2$) mounted in front of the whole HSI system in a reverse configuration, with the rear lens facing outward (figure 1(B)). The TWINS interferometer, even though particularly compact, has a non-negligible thickness (50 mm), mainly for mechanical support. Due to this, the TWINS could not be placed exactly in the back focal plane of the objective, considering that its principal planes are internal. The second lens is a 25 mm focal lens objective (Thorlabs MVL25M23) placed at a short distance from the TWINS, forming an optical configuration referred to as a *quasi*-4 f optical system, as shown in figure 1(B). In this case, the FOV, set by the size of the sensor (acting as the field stop of the optical system), is greatly reduced to 12 mm, while the working distance of the whole system, which is equivalent to the flange focal distance of the reversed Nikon objective, is 46.5 mm. The overall spatial resolution, calculated from the edge response function of a calibration slide, is 30 μm. Finally, note that the effective angular aperture of the optical system cannot be calculated as the ratio f/n of either the Nikon or the Thorlabs objectives. In fact, the system is (quasi) afocal and its aperture is better represented by the Numerical Aperture (N.A.) parameter, as in the case of

Table 1. Comparative table of the technical details for standard and macro-HSI systems.

	Number of lenses	Lens focal length	Total system size	FOV	Spatial resolution	Sample distance
Large FOV	1	25 mm	10×15 cm^2	>150 mm	>300 μm	>500 mm
Macro	2	25 mm + 50 mm	10×23 cm^2	13–20 mm	>30 μm	46.5 mm

microscope objectives. This parameter can be calculated from its definition: N.A. $=$ sin $\vartheta/2$, where ϑ is the acceptance angle for the rays emitted by any point of the object plane (figure 1(B)). Considering the clear aperture of the TWINS and the working distance of the system, the numerical aperture is N.A. $\cong 0.1$, which is comparable to that of low magnification microscope objectives with a long working distance. Table 1 summarises and compares the main technical details of the standard large field and of the macro-HSI systems.

2.2. Protocol for HSI measurements

2.2.1. Reflectance HSI

Both acquisitions performed on the model painting were done by illuminating the sample with a halogen lamp (Dedolight DLH4 Sportlight, irradiance of 140 W m^{-2} corresponding to 12 Klux) that was placed off-axis at an angle approximately of 45° with respect to the detection axis in order to minimize specular reflections: the distance of the lamp from the sample surface was ∼1 m for the large FOV configuration and ∼20 cm for the macro one. The macro-HSI acquisitions performed on the case studies were done by illuminating the sample with a different halogen lamp (Leica CLS 100 X Microscope Cold Light Source, irradiance of 3 W m^{-2} corresponding to 630 lux) fitted with an infrared filter to remove the IR components and reduce the thermal load and equipped with two optical fibres that can be easily oriented. Similarly, the two optical fibres were placed at the sides of the sample, at an angle of 45° with respect to the collection to minimize reflections. In all cases, polarisers were placed in front of the illumination source and oriented to reduce even further possible specular reflections. The FT-HSI measurement requires the acquisition of the interference images as a function of the delay imposed by the interferometer [23]. In the present research, the protocol consisted in the acquisition of 200 frames at variable phase delays from −54 fs to +54 fs by steps of 0.54 fs at the wavelength of 600 nm, resulting in a spectral resolution of ∼4 nm. The integration time for each frame was set to fill the camera dynamic range and was in the order of tens of milliseconds (40 ms for the large FOV acquisitions, 20–50 ms for the macro ones). A full acquisition takes less than 1 min, the limiting element being the translation stage movement that requires a precise control of its motion. In the large FOV measurement, the spatial illumination inhomogeneity was corrected by imaging also a Lambertian standard (X-rite White Balance) placed in the object plane, and calibrated with an absolute-standard-white reference (Labsphere Spectralon®, >95% total reflectance in the range 250–2500 nm) arranged in the FOV. In the case of the macro acquisition, thanks to the limited size of the FOV, it was sufficient to place only the absolute-standard-white reference at the object plane, enabling us to obtain simultaneously both white calibration and flat-field correction of the entire FOV.

2.2.2. Fluorescence HSI

To stimulate fluorescence from biofilms on stone samples and from dyed wool, we used two different excitation sources. In the first case, a widefield illumination was obtained by collimating the light emitted by an LED source at 623 nm (Thorlabs SOLIS-623 C) with 2 condenser lenses (a one-inch aspheric lens with $f = 16$ mm and a two-inch lens with $f = 60$ mm). The light was then refocused with a third lens with $f = 200$ mm to an area of about 4 cm in diameter and reached the sample with a power of 120 mW after passing through a band pass filter centred around 593 nm (BrightLine® single-band bandpass filter). Optical fluorescence from the biofilms was then filtered in the detection path with a long pass filter with edge at 650 nm (Thorlabs FELH650). In the case of tinted wool, the excitation light was the second harmonic of a Nd:YAG laser ($\lambda = 532$ nm, 1 mW, FTSS 355–50 CryLas GmbH). To obtain uniform illumination, the beam was coupled to a multimode silica fibre with a 600 μm core, and a magnified image of the fibre output tip was projected on the sample through a Galilean telescope. Since the field at the output surface of the fibre is uniform, the optical system enabled flat-top circular illumination with a diameter of about 2 cm. The emission from the sample was filtered along the detection path with a long pass filter at 550 nm (Thorlabs, FELH550). In both cases, the illumination axis was placed at approximately 60° with respect to the detection one to minimize specular reflections and to avoid clipping the illumination cone with the objective volume. The acquisition protocol was the same as the reflectance one, while the exposure time was increased to about 1 s to fill the camera dynamic range, resulting in an overall acquisition time of less than 5 min to collect the

entire HSI dataset. Finally, to maintain the same depth of field, the aperture of the optical system was kept the same as the reflectance measurement.

Reflectance and Fluorescence HSI datasets were analysed with home-made scripts written under the MATLAB environment.

2.3. Description of the case studies

To showcase the versatility of the macro-HSI configuration and demonstrate its capability to perform multimodal experiments, we tested our system on two case studies, in which we acquired both the reflectivity and the fluorescence dataset of the same FOV.

In the first case study, limestone samples colonized by cyanobacteria were used to explore the capability of the macro-HSI system to detect traces of the presence of the cyanobacterial biofilm and its biological activity by exploiting the autofluorescence of the bacterial photosynthetic pigments [28]. The accurate understanding of the exact role of the biofilm on stone heritage is crucial for the management of stone heritage, which calls for new non-invasive, portable diagnostics methods. In subaerial biofilms (SABs), microorganism photosynthetic pigments grow as colourful complex sessile communities on mineral surfaces exposed to the atmosphere, such as the stone surfaces of historic buildings [29]. The SAB pigments are influenced by the nature of the substrate [30, 31] as well as by the location and environmental conditions [32]. Since the physiological state of photosynthetic microorganisms is closely related to the activity of the photosynthetic system, any variation in their spectroscopic properties indicates changes in the microbial community physiology [29, 33]. SAB sample on limestone was prepared according to the protocol reported by Villa *et al* [34] and detailed in supplementary information [35, 36].

As a second case study, we considered samples with a high degree of three-dimensionality to highlight the effectiveness of the system to be used even in the presence of inhomogeneity of the sample surface, as in the case of textile heritage. Indeed, textile artefacts are susceptible to degradation, which poses considerable challenges to conservation. The degradation process of dyes, induced by factors such as light, heat, humidity and biological agents, significantly affects the appearance and integrity of dyed materials, causing fading and alteration of colours. To this end, the identification and study of dyes, as well as their ageing processes and chemical degradation pathways, are fundamental to achieving effective conservation strategies [37]. Micro-invasive techniques, such as high-performance liquid chromatography (HPLC), Raman-SERS, and FTIR spectroscopies, can be used to precisely identify the dye on the thread. However, recent years have seen a growing interest in the development and application of non-invasive spectroscopy and imaging techniques to study historical textiles [38–40]. In this context, we tested our approach on the study of wool yarns dyed with Rhodamine B artificially aged for different times (as described in supplementary information), with the aim of detecting and localising traces of the dye used even on a very discoloured sample and assessing the dyeing conditions without unravelling the thread.

3. Results and discussion

3.1. Characterisation of the system

To assess and compare the HSI capabilities of the two optical configurations, i.e. large FOV and macro, we studied the quality of the interferograms by performing a ray-tracing simulation with Ansys Zemax OpticStudio (details in supplementary information). To this purpose, the two objective lenses were modelled as Gaussian doublets of equivalent effective focal lengths, since no information on their optical design was provided by the manufacturers.

In the first simulation, aimed at studying the image quality of the two optical configurations, the TWINS interferometer acts only as a transparent plate that sets the aperture stop of the optical system. Consequently, it was simulated as an iris of 10 mm in diameter (which is the size of the smallest BBO plate in the TWINS interferometer). For the large FOV system the TWINS was placed at 70 mm before the 25 mm camera lens. The ray tracing simulation (supplementary figure S1(A)), shows a sharp image, confirming that the TWINS does not affect the quality of the optical system. Conversely, when working with the macro-HSI configuration, the non-ideality of the implemented quasi-4 f optical system has the effect of partially vignetting the image (supplementary figure S1(B)). However, the vignetting is limited to the vertices of the object (simulated as a square of 12 mm side), while the overall image quality is unaffected, as demonstrated by the previously mentioned edge response function. It should also be noted that, if the distance between the two objectives and the iris were optimal, vignetting would not be present.

Then, a second simulation assessed the interferometric contrast by replacing the iris with two α-BBO slabs with orthogonal optical axes (2.4 mm of thickness and 10 mm of lateral size) to model the TWINS described in Perri *et al* [23]. Notwithstanding the same thickness of the birefringent slabs, the ray bundles from the point sources in the object plane travels through the interferometer at a different angle and

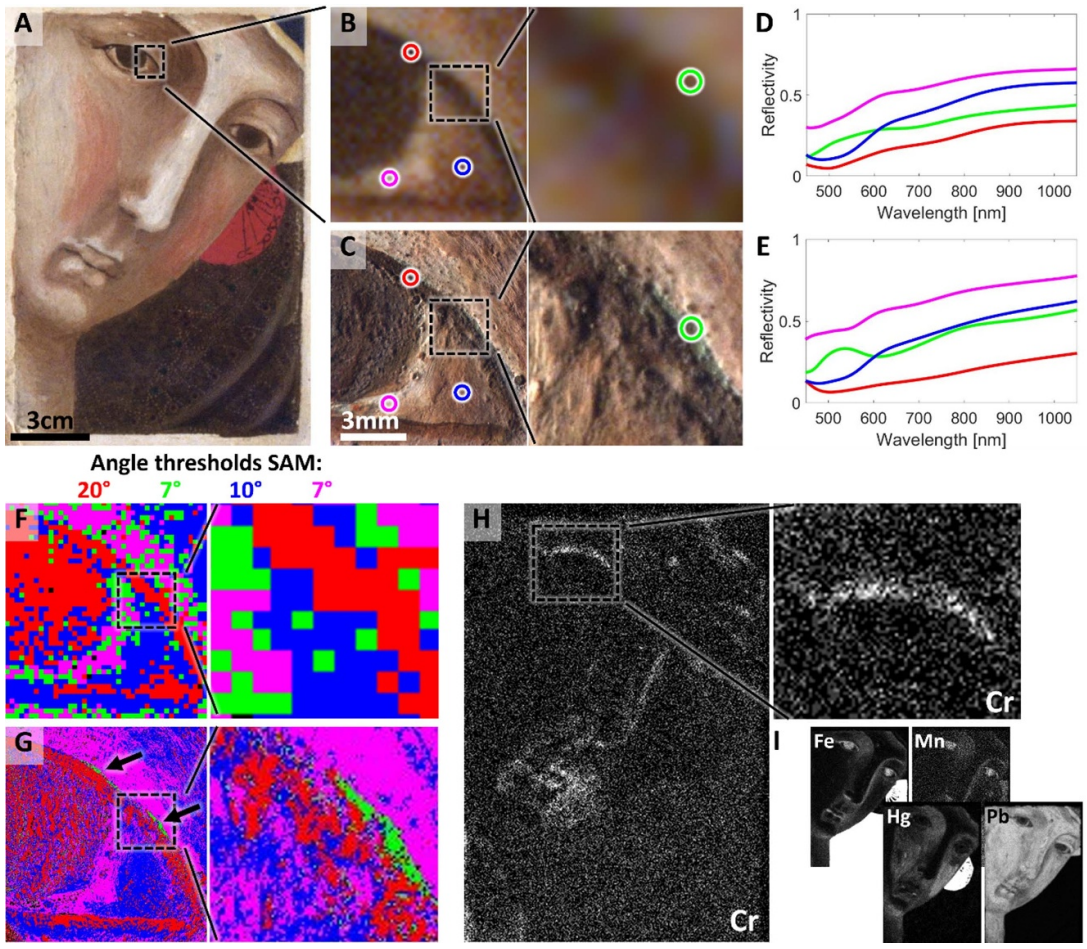

Figure 2. Comparison between large FOV HSI and macro-HSI acquisitions. (A) Colour RGB image retrieved from the reflectance spectral hypercube of the large FOV measurement. (B) Eye detail of panel (A) with a further zoom on the right panel. (C) Colour RGB image retrieved from the reflectance spectral hypercube of the macro measurement of the same eye detail of panel (B). (D) Reflectivity spectra obtained from the regions indicated by circles in panel (B). (E) Reflectivity spectra obtained from the regions indicated by circles in panel (C). (F) SAM analysis on the eye detail of the large FOV reflectance spectral hypercube with reference spectra shown in panel (D). (G) SAM analysis on the macro reflectance spectral hypercube with reference spectra shown in panel (E); the black arrows indicate the small clusters similar to the green spectrum in panel (E). (H) Cr element distribution retrieved from the XRF map, with the zoom on the eyelash detail. (I) Further elements distribution retrieved from the XRF mapping.

experience a different optical path length in the TWINS. Using monochromatic light at the Fraunhofer D-line (588 nm) the simulation produces a spatial interferogram in the image plane shown in figure 1(C). The contrast of these spatial fringes is related to the contrast in the temporal interferograms at each pixel. Hence, this pattern is a good indication of the quality of the overall FT-HSI system. As expected, the contrast is lower than the ideal value of 100% because the rays in the bundles coming from each point in the FOV (here we provide three exemplary points) are not parallel. Their small angular dispersion produces a phase dispersion $\Delta\varphi$ that is responsible for a decrease in the fringe visibility, as shown in figure 2(c) of Perri *et al* Let us now consider the macro-HSI system and its spatial interferogram displayed in figure 1(D). Since the ray tracing for the same exemplary points in the FOV shows parallel ray bundles at the TWINS, a very high contrast, ideally 100%, is obtained.

3.2. Comparison between standard and macro configurations

To demonstrate the benefit of using the hyperspectral camera in macro mode to study details in an artwork, we compared reflectivity measurements of a model painting (detailed in supplementary information) acquired with both large FOV and macro configurations: the detected areas correspond to the entire artwork and a detail in the eye region, respectively. Figure 2(A) shows the colour RGB image retrieved from the reflectance HSI dataset of the large FOV measurement; a subset of the same data around the eye area is reported in figure 2(B). The same area acquired with the macro-HSI is reported in figure 2(C); the macro-HSI inevitably leads to a clear improvement in the overall image quality, which allows for the more precise identification of areas where pigments of different spectral reflectivity and composition are present. To compare the two measurements, we tested the ability to spatially segment the characteristic spectral

signatures in the two datasets. This segmentation has been performed through the Spectral Angle Mapper (SAM) analysis on the base of four spectral references obtained from areas with different reflectivity: two regions in the eye sclera (see blue and magenta circles highlighted in figure 2 panels (B) and (C)), parts including the eyelash, the pupil and the iris (red circle) and a small area in the upper part of the eyelash (green circle). A similarity map is obtained for each reference spectrum by setting a proper angular threshold (indicated in figure 2). In this investigation, the macro-HSI system outperforms the large FOV HSI measurement in both reference spectra selection and in the generation of the composite SAM image, generated by merging the related similarity maps. In fact, the selected spectra from the macro dataset are purer than those obtained from the large FOV measurement, in which the spectral content from one colour area mixes with contributions from nearby regions (compare panels (D) and (E) in figure 2); moreover, the spatial segmentation resulting from the macro is more precise and detailed, allowing for the resolution of small clusters of different material (compare panels (F) and (G) in figure 2). In particular, it is noticeable the identification in the macro dataset of the small areas highlighted in green in the SAM map of figure 2(G) that are not distinguishable in the large FOV measurement when applying the same analysis (figure 2(F)) but, nevertheless, they are crucial to understand the composition of the painting as they represent small emerging clusters of a hidden layer. This statement can be inferred by considering their related spectrum (green line in figure 2(E)), which is in accordance with the reflectivity of chrome oxide green pigment [41], and by comparing the macro reflectivity results with an XRF mapping analysis (figures 2(H) and (I)), where the presence of chromium (Cr) element is detected in the region of the eyelash (figure 2(H)). This outcome clearly shows the importance of macro-HSI in accessing small features in samples like artworks through a non-invasive experiment, while retaining and relating details to the larger spatial contest.

3.3. Application to the study of flat samples: biofilm on limestone

We demonstrate the efficacy of our multimodal macro-HSI on a SAB sample prepared on limestone as detailed in supplementary information. A standard photograph of the overall stone is reported in figure 3(A), where the area analysed with the macro-HSI [42] is highlighted by the red box. Figure 3(B) shows the RGB image retrieved from the reflectance HSI data, where fine details of the surface of the stone sample can be noticed. Even though the presence of the biofilm is not obvious by eye inspection, by extracting the reflectance spectra of different areas it is possible to discern regions with diverse spectral features, as illustrated in figure 3(C). Further information can be obtained by computing the first derivative of the reflectance spectra, an operation which is not always possible with standard HSI methods, but which is straightforward with spectra arising from the FT approach (as it intrinsically includes a spectral low-pass filter. The first derivative (see figure 3(C), dashed lines) enhances the rapid change in reflectivity and hence highlights small differences between imaged materials. The maps of the derivatives at the peak wavelength of the 3 previously identified spectra are shown in figure 3(D); their fusion enables the generation of the false-RGB image of the sample shown in figure 3(E). The analysis enables the identification of three main areas with distinct spectral features. The false colour image highlights the existence of a round area, invisible in the photographic image and weakly visible in the macro RGB one, surrounded by a second patchy region corresponding to the greenish areas. The third area (blue in the false colour image) corresponds to mainly un-biocolonized surface [43]. The same sample portion was then analysed with fluorescence macro-HSI. To note, the dataset was acquired with the same aperture as the reflectance so that the depth of field is kept the same. This also enables the possibility to use the two datacubes in combination and correct the fluorescence data for self-absorption with the Kubelka–Munk model [44]. Figure 3(F) reports a false RGB image obtained from the fluorescence dataset corrected for the self-absorption (blue 640–655 nm, green 665–685 nm, red 720–800 nm). This image reveals the wide presence of cyanobacteria biofilm on the stone thanks to the high sensitivity of the fluorescence that facilitates the observation even of traces of the biofilm. This is also evidenced by the spectra retrieved from the circled areas and reported in figure 3(G), with special attention to the grey one, which was taken in an area where supposedly there was no biofilm. The spectra extracted from the circled areas correspond to those where the microbial community shows a varied physiological condition. In fact, the observed emission is due to the fluorescence of the two photosystems (PS) PSI and PSII, with the peak around 710 nm being an indicator of the photosynthetic activity of the two PS [45, 46] and the peak at 685 nm mainly corresponding to PSII and the Chlorophyll-a (Chl-a) subunit maximum emission [45, 47]. The zones with a stronger red hue in the false RGB image and represented by the red spectrum in figure 3(G), disclose a strong emission shoulder at 710 nm, peculiar of intact cells and originated by the efficiency of the energy transfer between all components of the energy transfer chain, from the initially photoexcited phycobiliprotein to the reaction centre of photosystems PSI and PSII [33]. These regions also match the greenest areas in the reflectivity image. On the other hand, the bluer areas (represented by the blue spectrum in figure 3(G)), correspond to a blue-shifted emission, that can be associated to regions with high Chl-a degradation [48, 49]. These areas also match those that are more discoloured in the reflectance map.

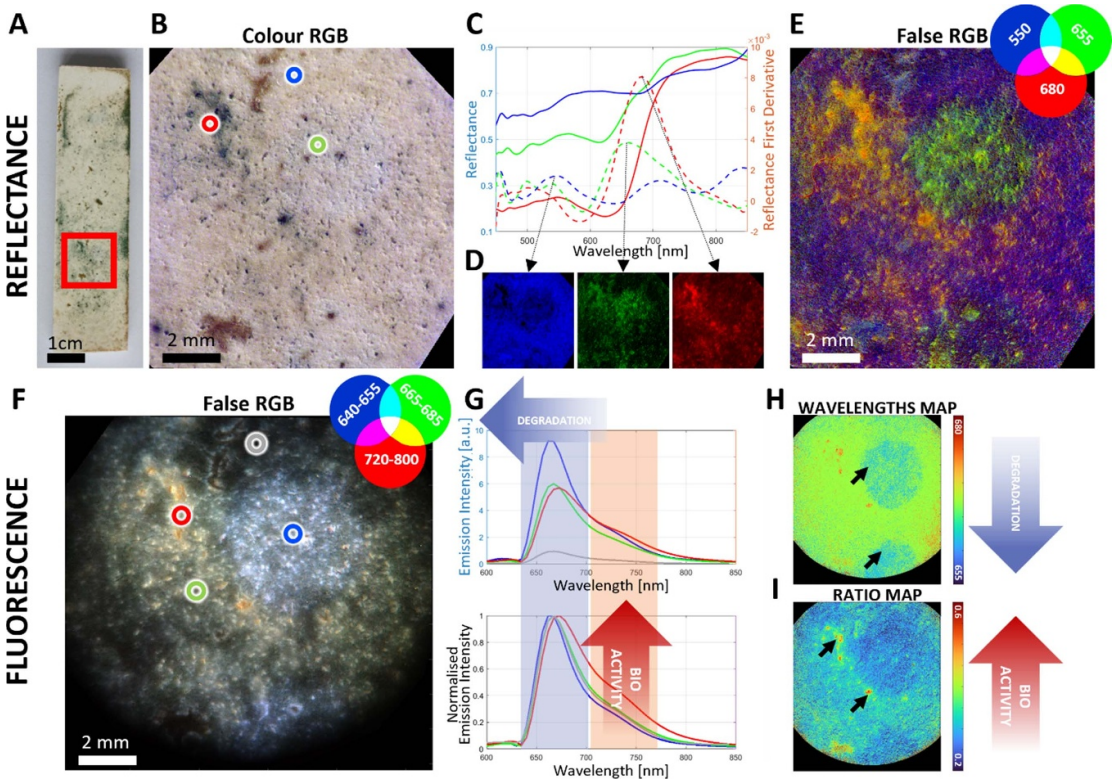

Figure 3. Biofilm analysis. (A) Standard photograph of the limestone sample colonized with the biofilm, where the red box shows the area analysed with the macro-HSI. (B) Colour RGB image retrieved from the reflectance spectral hypercube obtained with the macro-HSI. (C) Reflectance spectra of the regions circled in (B) (solid line) and the correspondent first derivatives (dashed line). (D) Colour-coded maps retrieved at the pick wavelength of the first derivative of the reflectance spectra. (E) False RGB image of the sample obtained by combining the 3 derivative image in (D) (colour-code shown on the top right). (F) False RGB image retrieved form the fluorescence spectral hypercube (colour-code shown on the top right). (G) Spectra of the regions circled in (F) (top panel) and the correspondent normalized spectra (bottom panel). The two regions of interest for the related to the degradation and the photoactivity are highlighted in blue and red, respectively. (H) Map of the peak wavelength of the fluorescent emission. The arrows indicate areas of higher degradation. (I) Map of the ratio between the emission at 710 nm and the maximum emission. The arrows highlight areas of higher photosynthetic activity.

To further enhance the visibility and readability of the data, we created a map of the peak wavelength of Chl-a emission (figure 3(H)) and a map of the ratio between the emission at 710 nm and the maximum spectral emission (figure 3(I)). From the first one we can easily determine where the biofilm is more degraded, as for example the areas indicated by the arrows, while from the second one we directly obtain information on the biofilm photosynthetic activity, where a ratio near to 1 corresponds to higher activity. An interesting aspect to pay attention to is that the red spots in this last image correspond to micro-fissures and porosity of the stone, like those indicated by the arrows, index of greater biofilm health in those more protected areas. Accordingly, it has been reported that carved surfaces are colonized more easily than smooth surfaces as the irregularities in the surface form anchoring sites for microorganisms, protect cells from hydrodynamic forces, and ensure them more water and nutrients [50].

3.4. Application to the study of three-dimensional samples: tinted wool yarn

We prove our instrument's ability to analyse even three-dimensional art objects by considering the study of dyed and artificially aged wool yarns. To increase the depth of field and make sure that the whole yarn thread was in focus, we took advantage of the high light collection throughput of our macro-HSI and reduced the size of the aperture stop of the optical system in the same manner for both reflectance and fluorescence datasets [42]. Figure 4(A) displays the colour RGB image reconstructed from the reflectance datacube (left panel) and the reflectance spectra associated to the circled areas (right panel), while figure 4(B) shows a zoom of the area highlighted in the previous figure with a dashed square. It is noteworthy that the fibres can be observed all at the same time with good resolution, and show differences in colour distribution, associated to the fading of the dye. Figure 4(C) presents the false RGB image retrieved from the fluorescence dataset (blue 550–570 nm, green 570–600 nm, red 600–750 nm) with the right panel displaying the normalized fluorescence spectra of the circled areas, while figure 4(D) is the zoom-in on the region highlighted by a dashed square in figure 4(C). This false RGB shows the striking variability of the spectral emission of the

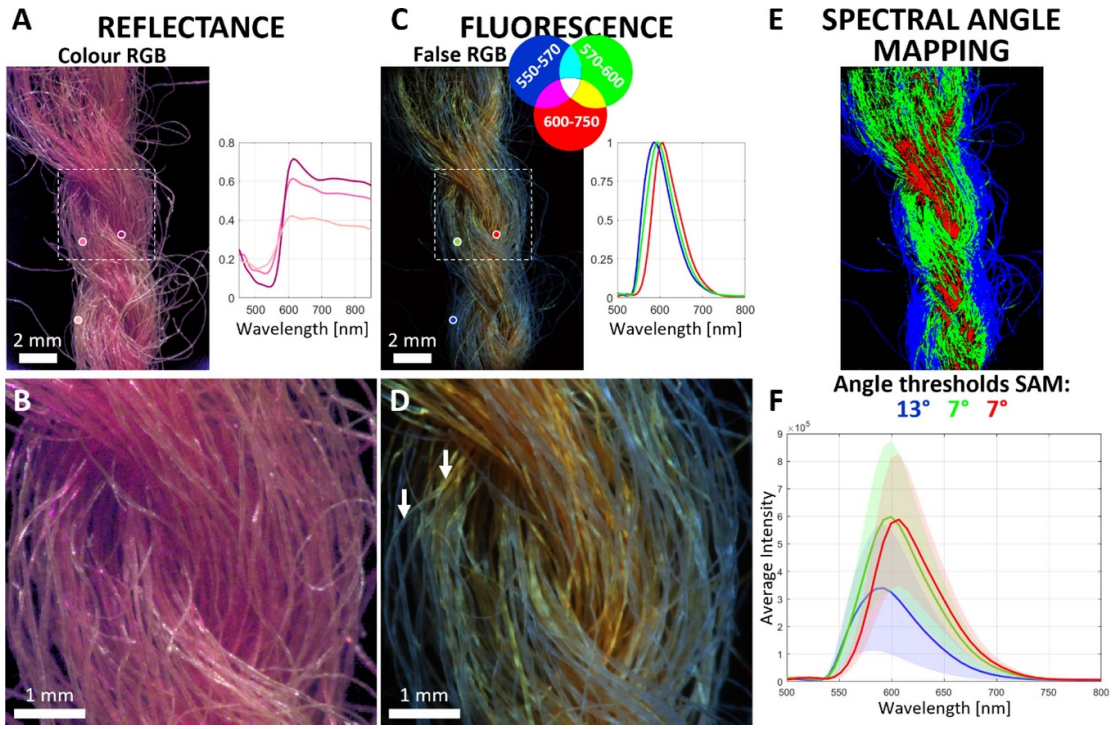

Figure 4. Aged dyed wool analysis. (A) Colour RGB image of the dyed wool thread after 160 h of artificial aging, retrieved from the reflectance spectral hypercube obtained with the macro-HSI together with selected reflectance spectra of the circled regions. (B) Zoomed in area defined by the dashed square in (A). (C) False RGB image retrieved form the fluorescence spectral hypercube (colour-code shown on the top right) with selected fluorescence spectra of the circled regions. (D) Zoomed in area defined by the dashed square in (C); the arrows highlight two zones of the same strand with different extent of discolouration. (E) Composite image generated by the SAM analysis performed on the fluorescence hypercube created using the reference spectra of the most discoloured area (blue, angle threshold of 13°), the best preserved one (red, angle threshold of 7°) and an intermediate (green, angle threshold of 7°). (F) Average spectra of the SAM clusters with the standard deviation.

rhodamine throughout the yarn, not only in intensity but also in spectral characteristics. It is remarkable that we can also notice that single strands have inhomogeneous discolouration, something that could not be noticed with standard analytical methods like HPLC or point-wise spectroscopies, which commonly only consider an average behaviour of the strand. When comparing to a microscopic approach, in the macro one we have many single fibres in the FOV that are all in focus and that can be considered singularly but in their framework. We performed SAM analysis on the base of 3 characteristic spectra that we obtained from the most discoloured area, the best preserved one and an intermediate, and the results are presented in figure 4(E), which also reports the angle threshold used. Figure 4(F) illustrates the average spectra of the SAM clusters with the standard deviation, highlighting a blue-shift in peak wavelength and a reduction in fluorescence emission for those fibres that are positioned on the outer part of the thread. The blue-shift is due to the degradation of the rhodamine [51] with the aging, which is expected to be higher in the outer part of the thread. Further to the capability of detecting small differences in dye condition, it is worth mentioning that the high sensitivity of the method allows for the detection of even traces of degraded dye from highly discoloured wool yarns. In addition, supplementary figure S2 shows the analysis of a thread that was not aged, one that was aged for 20 h and one that was aged for 305 h. Of particular interest is the fact that we can detect even small variations of the degraded dye in the 20 h sample, as well as areas in the 305 h in which the spectral characteristics of the degraded Rhodamine B can still be detected even though fading and degradation strongly occurred.

4. Conclusions

We have presented the development of a macro-HSI system that proved effective for the study of both reflectance and fluorescence properties of a variety of samples on the same FOV sequentially. The design of the setup is based on a two-lens optical system that allows a rapid switch between a large FOV and a macro one. We demonstrated how the devised configuration provides high visibility fringes, while keeping good imaging quality. The macro-HSI system complements the set of hyperspectral devices available in our laboratory, filling the gap between microscopy and large FOV. Indeed, in conservation science, the traditional

approach to works of art addresses either the entire object, typically *in situ*, or micro-fragments analysed in the laboratory. However, there are cases in which a close-up study of the surface of large objects or entire small artworks are needed for identifying compositional or degradation materials at an intermediate scale with respect to the mentioned methods. Through the analysis performed on the model painting, this study highlights the significance of employing a macro system when it enabled access to small details while preserving their relationship within a larger spatial context. This also allowed detecting the presence of materials that otherwise would not be identified with a wide field analysis, and that was confirmed by XRF mapping.

Furthermore, our system proved its capability to acquire multimodal datasets, since it is possible to easily switch from the reflectance to the fluorescence configuration, while looking at the very same FOV. This enabled us to combine the two pieces of information and even use one dataset to correct for self-absorption of the sample. More specifically, the measurements permitted the mapping of the distribution of photosynthetic cyanobacterial pigments on a limestone substrate by both reflectance and fluorescence data, leading to the detection of traces of biofilms on porous surfaces and to the identification of areas with different photosynthetic activity and therefore physiological state.

Moreover, we have shown the capability of the system to record datasets from both flat and three-dimensional artworks, since thanks to the high collection efficiency we can reduce the aperture of the optical system and extend the depth of field. This is a significant advantage for capturing comprehensive spatial information while maintaining the coherence of the multimodal datasets. The approach has been applied to the study of dyed wools at different aging stages. The multimodal imaging approach also reveals the presence of volumetric inhomogeneities in the wool yarns induced by aging. These would hardly be characterized with standard point-wise methods that can precisely analyse small portions of the sample but lose the heterogeneity of the whole.

Looking ahead, we aim to further enhance the usability of our system by developing a compact, fully portable version that can be easily transported to field locations. This portability will broaden the range of scenarios in which our macro imaging system can be applied, making it an even more valuable tool.

Data availability statement

The data that support the findings of this study are openly available at the following URL/DOI: https://doi.org/10.5281/zenodo.10804406.

Acknowledgments

The authors acknowledge financial support by the European Union's NextGenerationEU Programme with the I-PHOQS Infrastructure [IR0000016, ID D2B8D520, CUP B53C22001750006] "Integrated infrastructure initiative in Photonic and Quantum Sciences. C M acknowledges support by European Union's European Innovation Council (EIC), TROPHY PATHFINDER-OPEN-01 101047137.

ORCID iDs

Benedetto Ardini https://orcid.org/0000-0003-2188-5867
Matteo Corti https://orcid.org/0009-0002-5056-9548
Marta Ghirardello https://orcid.org/0000-0002-0179-5859
Alessia Di Benedetto https://orcid.org/0009-0000-5966-0052
Letizia Berti https://orcid.org/0000-0002-6508-2989
Cristina Cattò https://orcid.org/0000-0002-3709-1802
Sara Goidanich https://orcid.org/0000-0001-6774-1805
Giorgia Sciutto https://orcid.org/0000-0002-0608-8379
Silvia Prati https://orcid.org/0000-0002-9974-731X
Gianluca Valentini https://orcid.org/0000-0002-6340-3021
Cristian Manzoni https://orcid.org/0000-0002-4169-8869
Daniela Comelli https://orcid.org/0000-0002-7175-2870
Alessia Candeo https://orcid.org/0000-0001-9597-3056

References

[1] Madariaga J M 2015 Analytical chemistry in the field of cultural heritage *Anal. Methods* **7** 4848–76
[2] Anglos D, Georgiou S and Fotakis C 2009 Lasers in the analysis of cultural heritage materials *J. Nano Res.* **8** 47–60

[3] Bitossi G, Giorgi R, Mauro M, Salvadori B and Dei L 2005 Spectroscopic techniques in cultural heritage conservation: a survey *Appl. Spectrosc. Rev.* **40** 187–228
[4] Tan H, Tian H, Verbeeck J, Monico L, Janssens K and Van Tendeloo G 2013 Nanoscale investigation of the degradation mechanism of a historical chrome yellow paint by quantitative electron energy loss spectroscopy mapping of chromium species *Angew. Chem.* **125** 11570–3
[5] Comelli D, MacLennan D, Ghirardello M, Phenix A, Schmidt Patterson C, Khanjian H, Gross M, Valentini G, Trentelman K and Nevin A 2019 Degradation of cadmium yellow paint: new evidence from photoluminescence studies of trap states in Picasso's Femme *(époque des 'demoiselles d'Avignon') Anal. Chem.* **91** 3421–8
[6] de la Rie E R, Michelin A, Ngako M, Del Federico E and Del Grosso C 2017 Photo-catalytic degradation of binding media of ultramarine blue containing paint layers: a new perspective on the phenomenon of 'ultramarine disease' in paintings *Polym. Degrad. Stab.* **144** 43–52
[7] Alfeld M *et al* 2013 Revealing hidden paint layers in oil paintings by means of scanning macro-XRF: a mock-up study based on Rembrandt's 'an old man in military costume *J. Anal. At. Spectrom.* **28** 40–51
[8] Gasanova S, Bakirtzis N and Hermon S 2017 Non-invasive sub-surface analysis of the male portrait underlying the Titian's Studio *Ecce Homo Heritage Sci.* **5** 33
[9] Comelli D *et al* 2016 The meteoritic origin of Tutankhamun's iron dagger blade *Meteorit. Planet. Sci.* **51** 1301–9
[10] Picollo M, Cucci C, Casini A and Stefani L 2020 Hyper-spectral imaging technique in the cultural heritage field: new possible scenarios *Sensors* **20** 2843
[11] Cucci C, Delaney J K and Picollo M 2016 Reflectance hyperspectral imaging for investigation of works of art: old master paintings and illuminated manuscripts *Acc. Chem. Res.* **49** 2070–9
[12] Delaney J K, Thoury M, Zeibel J G, Ricciardi P, Morales K M and Dooley K A 2016 Visible and infrared imaging spectroscopy of paintings and improved reflectography *Heritage Sci.* **4** 6
[13] Capobianco G, Bonifazi G, Prestileo F and Serranti S 2014 Pigment identification in pictorial layers by HyperSpectral Imaging *Proc. SPIE* **9106** 30–41
[14] Delaney J K, Dooley K A, van Loon A and Vandivere A 2020 Mapping the pigment distribution of Vermeer's Girl with a Pearl Earring *Heritage Sci.* **8** 4
[15] Delaney J K, Zeibel J G, Thoury M, Littleton R, Palmer M, Morales K M, Rie E R D L and Hoenigswald A 2010 Visible and infrared imaging spectroscopy of Picasso's Harlequin musician: mapping and identification of artist materials in situ *Appl. Spectrosc.* **64** 584–94
[16] Albano M, Ghirardello M, Fiocco G, Manzoni C, Malagodi M and Comelli D 2021 Complementary mapping techniques to characterize the wood finish of musical instruments *Eur. Phys. J. Plus* **136** 1054
[17] Gomez Lobon M *et al* 2023 A study of cadmium yellow paints from Joan Miró's paintings and studio materials preserved at the Fundació Miró Mallorca *Heritage Sci.* **11** 145
[18] Radpour R, Gates G A, Kakoulli I and Delaney J K 2022 Identification and mapping of ancient pigments in a Roman Egyptian funerary portrait by application of reflectance and luminescence imaging spectroscopy *Heritage Sci.* **10** 8
[19] Dooley K A, Chieli A, Romani A, Legrand S, Miliani C, Janssens K and Delaney J K 2020 Molecular fluorescence imaging spectroscopy for mapping low concentrations of red lake pigments: van Gogh's painting the Olive Orchard *Angew. Chem., Int. Ed.* **59** 6046–53
[20] Moreau R, Calligaro T, Pichon L, Moignard B, Hermon S and Reiche I 2023 A multimodal scanner coupling XRF, UV–Vis–NIR photoluminescence and Vis–NIR–SWIR reflectance imaging spectroscopy for cultural heritage studies *X-ray Spectrom.* 1–11
[21] Wolfe W L 1997 *Introduction to Imaging Spectrometers* (SPIE)
[22] Davis S P, Abrams M C and Brault J W 2001 *Fourier Transform Spectrometry* (Elsevier)
[23] Perri A, Nogueira de Faria B E, Ferreira D C T, Comelli D, Valentini G, Preda F, Polli D, de Paula A M, Cerullo G and Manzoni C 2019 Hyperspectral imaging with a TWINS birefringent interferometer *Opt. Express* **27** 15956
[24] Ardini B *et al* 2023 High-throughput multimodal wide-field Fourier-transform Raman microscope *Optica* **10** 663
[25] Candeo A, Nogueira de Faria B E, Erreni M, Valentini G, Bassi A, de Paula A M, Cerullo G and Manzoni C 2019 A hyperspectral microscope based on an ultrastable common-path interferometer *APL Photonics* **4** 120802
[26] Ghirardello M *et al* 2023 Time-resolved photoluminescence imaging for the mapping of weakly luminescent pigments in paintings *Eur. Phys. J. Plus* **138** 906
[27] Candeo A, Ardini B, Ghirardello M, Valentini G, Clivet L, Maury C, Calligaro T, Manzoni C and Comelli D 2022 Performances of a portable Fourier transform hyperspectral imaging camera for rapid investigation of paintings *Eur. Phys. J. Plus* **137** 409
[28] Roldán M, Ascaso C and Wierzchos J 2014 Fluorescent fingerprints of endolithic phototrophic cyanobacteria living within halite rocks in the atacama desert *Appl. Environ. Microbiol.* **80** 2998–3006
[29] Villa F, Wu Y-L, Zerboni A and Cappitelli F 2022 In living color: pigment-based microbial ecology at the mineral–air interface *Bioscience* **72** 1156–75
[30] Pinna D 2014 Biofilms and lichens on stone monuments: do they damage or protect? *Front. Microbiol.* **5** 76788
[31] Mugnai G, Borruso L, Wu Y-L, Gallinaro M, Cappitelli F, Zerboni A and Villa F 2024 Ecological strategies of bacterial communities in prehistoric stone wall paintings across weathering gradients: a case study from the Borana zone in southern Ethiopia *Sci. Total Environ.* **907** 168026
[32] Cattò C, Mu A, Moreau J W, Wang N, Cappitelli F and Strugnell R 2023 Biofilm colonization of stone materials from an Australian outdoor sculpture: importance of geometry and exposure *J. Environ. Manage.* **339** 117948
[33] Yu Grigoryeva N 2020 Studying cyanobacteria by means of fluorescence methods: a review *Fluorescence Methods for Investigation of Living Cells and Microorganisms* (IntechOpen) (https://doi.org/10.5772/intechopen.93543)
[34] Villa F, Pitts B, Lauchnor E, Cappitelli F and Stewart P S 2015 Development of a laboratory model of a phototroph-heterotroph mixed-species biofilm at the stone/air interface *Front. Microbiol.* **6** 1251
[35] Villa F, Ludwig N, Mazzini S, Scaglioni L, Fuchs A L, Tripet B, Copié V, Stewart P S and Cappitelli F 2023 A desiccated dual-species subaerial biofilm reprograms its metabolism and affects water dynamics in limestone *Sci. Total Environ.* **868** 161666
[36] Crispim C A, Gaylarde P M and Gaylarde C C 2003 Algal and cyanobacterial biofilms on calcareous historic buildings *Curr. Microbiol.* **46** 79–82
[37] Degano I, Biesaga M, Colombini M P and Trojanowicz M 2011 Historical and archaeological textiles: an insight on degradation products of wool and silk yarns *J. Chromatogr.* A **1218** 5837–47
[38] De La Codre H, Daniel F, Chapoulie R, Servant L and Mounier A 2021 Investigating the materials used in eighteenth-century tapestries from the three French royal manufactories: inputs of hyperspectral approaches *Eur. Phys. J. Plus* **136** 1193

[39] Dyer J, Tamburini D, O'Connell E R and Harrison A 2018 A multispectral imaging approach integrated into the study of Late Antique textiles from Egypt *PLoS One* **13** e0204699
[40] Borrego P and Vega C 2015 A new approach to the understanding of historic textiles *Greek and Roman Textiles and Dress: An Interdisciplinary Anthology* ed M Harlow and M L Nosch (Oxbow Books) pp 374–98
[41] Cultural Heritage Science Open Source – CHSOS (available at: https://chsopensource.org/chrome-green-k-44200/)
[42] Ardini B, Corti M, Ghirardello M, Di Benedetto A, Valentini G, Manzoni C, Comelli D and Candeo A 2024 Data underlying the paper titled "Enhancing hyperspectral imaging through macro and multi-modal capabilities" *Zenodo* (available at: https://zenodo.org/records/10804406)
[43] Ramil A, Vázquez-Nion D, Pozo-Antonio J S, Sanmartín P and Prieto B 2020 Using hyperspectral imaging to quantify phototrophic biofilms on granite *J. Environ. Inf.* **35** 34–44
[44] Verri G, Clementi C, Comelli D, Cather S and Piqué F 2008 Correction of ultraviolet-induced fluorescence spectra for the examination of polychromy *Appl. Spectrosc.* **62** 1295–302
[45] Harel Y, Ohad I and Kaplan A 2004 Activation of photosynthesis and resistance to photoinhibition in cyanobacteria within biological desert crust *Plant Physiol.* **136** 3070–9
[46] Brecht M, Radics V, Nieder J B, Studier H and Bittl R 2008 Red antenna states of photosystem I from synechocystis PCC 6803 *Biochemistry* **47** 5536–43
[47] Vermaas W F J, Timlin J A, Jones H D T, Sinclair M B, Nieman L T, Hamad S W, Melgaard D K and Haaland D M 2008 In vivo hyperspectral confocal fluorescence imaging to determine pigment localization and distribution in cyanobacterial cells *Proc. Natl Acad. Sci.* **105** 4050–5
[48] Polerecky L, Bissett A, Al-Najjar M, Faerber P, Osmers H, Suci P A, Stoodley P and de Beer D 2009 Modular spectral imaging system for discrimination of pigments in cells and microbial communities *Appl. Environ. Microbiol.* **75** 758–71
[49] Dartnell L R and Patel M R 2014 Degradation of microbial fluorescence biosignatures by solar ultraviolet radiation on Mars *Int. J. Astrobiol.* **13** 112–23
[50] Miller A Z, Sanmartín P, Pereira-Pardo L, Dionísio A, Saiz-Jimenez C, Macedo M F and Prieto B 2012 Bioreceptivity of building stones: a review *Sci. Total Environ.* **426** 1–12
[51] Reiß L, Thomas P and Sarah G 2022 The light aging behavior of daylight fluorescent paints: a colorimetric, photographic, Raman spectroscopic and fluorescence spectroscopic study *Heritage Sci.* **10** 171